Microfiber-Enabled In-line Fabry–Pérot Interferometer for High-Sensitive Force and Refractive Index Sensing

Shecheng Gao, Weigang Zhang, Zhi-Yong Bai, Hao Zhang, Wei Lin, Li Wang, and Jieliang Li

***Abstract*—A microfiber-enabled Fabry–Pérot interferometer (FPI) constructed by splicing a section of microfiber between two cleaved standard single-mode fibers (SMFs) with unique relative fiber cross section relationship has been proposed and experimentally demonstrated. The opening air cavity between the two SMF ends connected by the microfiber serves as an FP cavity and also a direct sensing head. The sensing characteristics of the FPIs with different cavity lengths and microfiber diameters have been studied. A force sensitivity as high as 167.41 nm/N ($\sim$200 pm/$\mu\varepsilon$) and a high refractive index (RI) sensitivity of 1330.8 nm/RIU (around a RI of 1.33) have been achieved by using the microfiber-based FPI with $\sim$21 μm cavity length and $\sim$44 μm microfiber diameter. Such a device has several merits such as simple configuration, compactness and reliability in operation owing to the extremely low thermal cross-sensitivities.**

***Index Terms*—Fabry–Pérot interferometer (FPI), force sensor, microfiber, optical fiber sensor, refractive index (RI) sensor.**

I. Introduction

FOR decades, fiber-optic sensors have been intensively investigated and widely applied in physical, chemical, and biomedical sensing fields due to their unique advantages such as simplicity, immunity to electromagnetic interference, corrosion resistance, and remote sensing capability. As two basic physical parameters of great importance for many applications [1]–[14], force and refractive index (RI) were successfully measured by fiber gratings [1], [2] and various in-fiber devices, including single-mode-multimode-single-mode structures [3], [4], fiber loops [5]–[7], Mach-Zehnder interferometers [7]–[10] and Fabry-Pérot interferometers (FPIs) [11]–[14]. The fiber sensors based on FPIs possess many advantages, such as simple configurations, compactness, stable performances, and endurance for high temperature and high pressure environments, etc. [11]–[28]. Amongst them, the extrinsic-FPI-based sensors have been much more extensively investigated owing to their low temperature sensitivity, ease of fabrication, and good practicability [15]–[28].

Various methods have been reported to fabricate the extrinsic-FPI in the past two decades, from bonding two cleaved fibers into a small-diameter tube [15], splicing a short segment of silica hollow-core fiber or hollow-core photonic crystal fiber between two single-mode fibers (SMFs) [16]–[21] to forming a spherical air micro-cavity by splicing a hollow-core crystal fiber with a SMF [19]–[21]. They are usually employed as strain and high temperature sensors. Undoubtedly, force sensing is also possible [20]. But, the extrinsic-FPIs formed with the above methods have low strain/force sensitivities. Moreover, they are unable to measure the RI for the sealed cavities. To address the limitation of the sealed cavities that liquid/gas samples could not flow in or out for real-time chemical/biochemical sensing, recently, various schemes including micro-machined open micro-notch cavity fabricated on the side of SMF [22], [23] or a single microfiber probe [24], [25] using femtosecond (fs) laser/focused ion beam, and drilling vertical micro-channels to the sealed air cavity using fs laser [26]–[28] have been proposed. Most of these devices show constant high RI sensitivities over a large dynamic range and have very low temperature cross-sensitivities, notwithstanding it is still inconvenient to load liquid samples and rinse the cavity. However, the micromachining process is complicated and costly, and moreover, they have rather low force sensitivity or even could not be used to measure the axial force.

With the increasing demands on high-performance miniaturized sensors, compact microfiber-based optical sensors with high sensitivities have also been developed [2], [29]–[31]. In this paper, a novel microfiber-enabled (MF-enabled) in-line FPI has been constructed by fusing a short section of microfiber between two standard SMFs with unique fiber cross section geometrical relationship which breaks the shackle of the supporting arms of presently reported interferometers comparable to the outer diameter of the standard SMF. The MF-enabled FPI configuration significantly differs from that of the extrinsic-FPI sensors previously reported in that the outer diameter of the microfiber is much smaller than the lead SMFs and the FP cavity with smooth surface is all-opening, thus to enhance force sensitivity and facilitate the liquid RI measurement. The experimental results show that the proposed MF-enabled FPI possesses a high RI sensitivity and low temperature cross sensitivity. And more

Manuscript received November 9, 2013; revised January 13, 2014 and March 3, 2014; accepted March 3, 2014. Date of publication March 5, 2014; date of current version April 3, 2014. This work was supported by the National Natural Science Foundation under Grants 11274181, 10974100, and 10674 075, the Specialized Research Fund for the Doctoral Program of Higher Education under Grant 20120 031110033, China., the Future Technology Research Project under Grant 10JCZDJC24300, and the Fundamental Research Funds for the Central Universities.

The authors are with the Key Laboratory of Optical Information Science and Technology, Institute of Modern Optics, Nankai University, Tianjin 300071, China (e-mail: gaosc825@163.com; zhangwg@nankai.edu.cn; bzy041217@126.com; haozhang@nankai.edu.cn; superwei02421@126.com; jane–1125@163.com; nkljl@126.com).

Color versions of one or more of the figures in this paper are available online at http://ieeexplore.ieee.org.

Digital Object Identifier 10.1109/JLT.2014.2310205

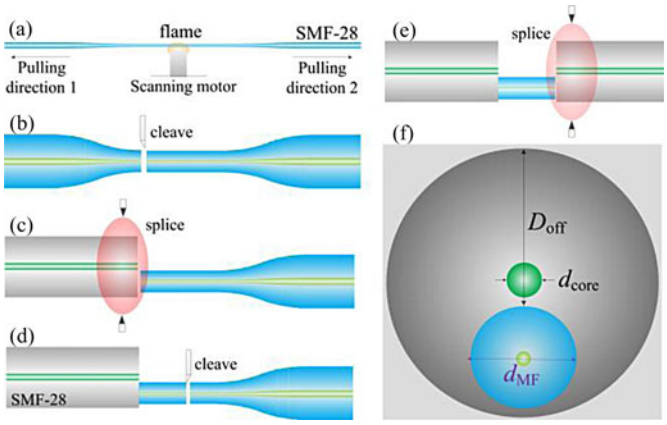

Fig. 1. (a)–(e) Fabrication procedures of MF-enabled FPI; (f) geometry relationship between the microfiber and SMFs at the splicing points.

importantly, it exhibits much higher force sensitivity than traditional in-fiber FPI sensors.

II. Fabrication

To fabricate the proposed sensor, a section of microfiber cut from a fiber taper waist is spliced between two sections of standard SMFs with designed fiber facet offset using a commercial fusion splicing machine. The fabrication procedures shown in Fig. 1(a)–(e) include five steps: tapering SMF, cleaving the fiber taper (microfiber, MF) and SMF, splicing the cleaved MF and SMF with designed relative cross section position, cleaving the MF to a desired length, and finally splicing to other SMF tip with the same relative cross section position as the first joint.

First, as shown in Fig. 1(a), the standard SMF (Corning, SMF-28e) is tapered using the flame-brushing technique [32]. The MF diameter can be controlled by adjusting related parameters including the elongation speed and the elongation length under the constant flame traversal length. Here, we taper the SMFs with ∼44 and ∼56 μm taper waist diameters and about 25 mm waist length. Secondly, cleave the fiber taper (MF) into two segments at its waist with flat and smooth end interfaces, as illustrated in Fig. 1(b). The third step, the MF pigtail with a long length is spliced with one cleaved SMF, as shown in Fig. 1(c). During the splicing process, the microfiber is stepped approaching to SMF by using a fiber splicer (FITEL S178 A, in manual operation mode) with core calibration as shown in Fig. 1(f). The splicing process is very important because it must be ensured that the SMF end face has no obvious deformation and the MF does not touch the SMF core. After splicing the first joint, we cleaved the microfiber with designed length assisted by a linear translation stage, as shown in Fig. 1(d). At last, the microfiber tip was then placed in the splicer at its original position with the assistance of the enlarged image in the monitoring window of the fiber splicer, and the second SMF tip was calibrated referenced to the microfiber tip, as shown in Fig. 1(f). The MF is completely located outside the SMF core edges by about 5 μm to acquire relatively large mechanical strength, and meanwhile to ensure good quality interferometric effect between the SMF core-facets. The second splicing joint is controlled to make sure

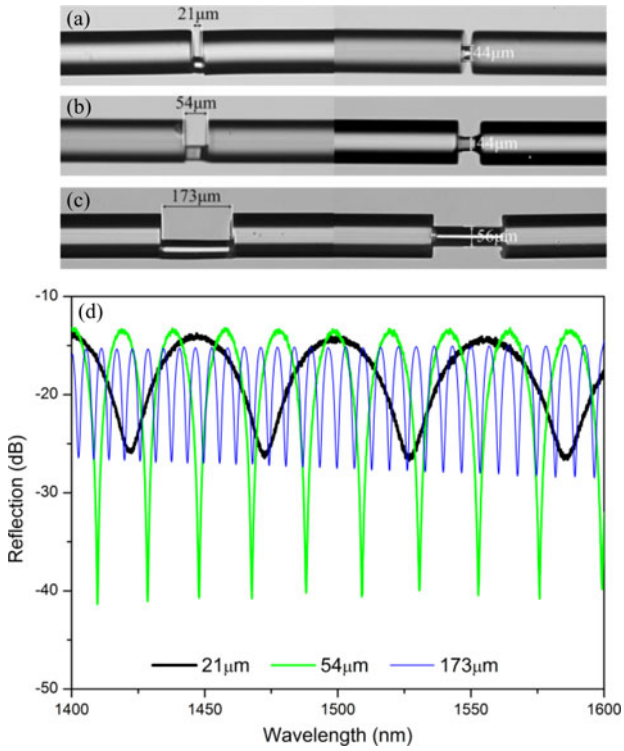

Fig. 2. (a)–(c) Side view and top view microscopic images of the FPIs with different cavity lengths and different microfiber diameters; (d) Reflection spectra of the MF-enabled FPIs corresponding to (a)–(c).

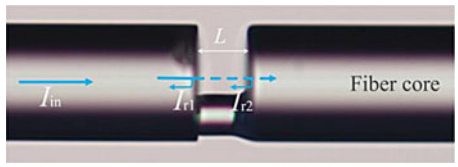

Fig. 3. Schematic diagram of the MF-enabled FPI.

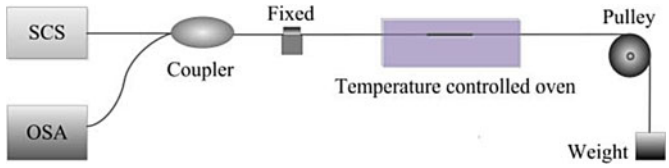

Fig. 4. Schematic experimental setup of the MF-enabled FPI sensing system.

that the microfiber and the output SMF possess the same relative offset situation as their input counterpart as shown in Fig. 1(e). Experiments show that the splicing process of second splicing joint is not as strict as the first joint, and the slight contact between the MF and SMF core does not seriously affect the device performances. The splicing parameters are as follows: the discharge electric intensity parameter is set to "90" and the duration time is respectively set to 150 ms and 200 ms for splicing the ∼44 μm- and ∼56 μm-diameter MFs with the SMFs. The discharge is applied for the SMF with an offset of ∼60 μm as shown in Fig. 1 (c) and (e). By adjusting the linear translation stage, MF-enabled FPIs with different cavity lengths could be easily achieved. Fig. 2(a)–(c) show the microscopic images

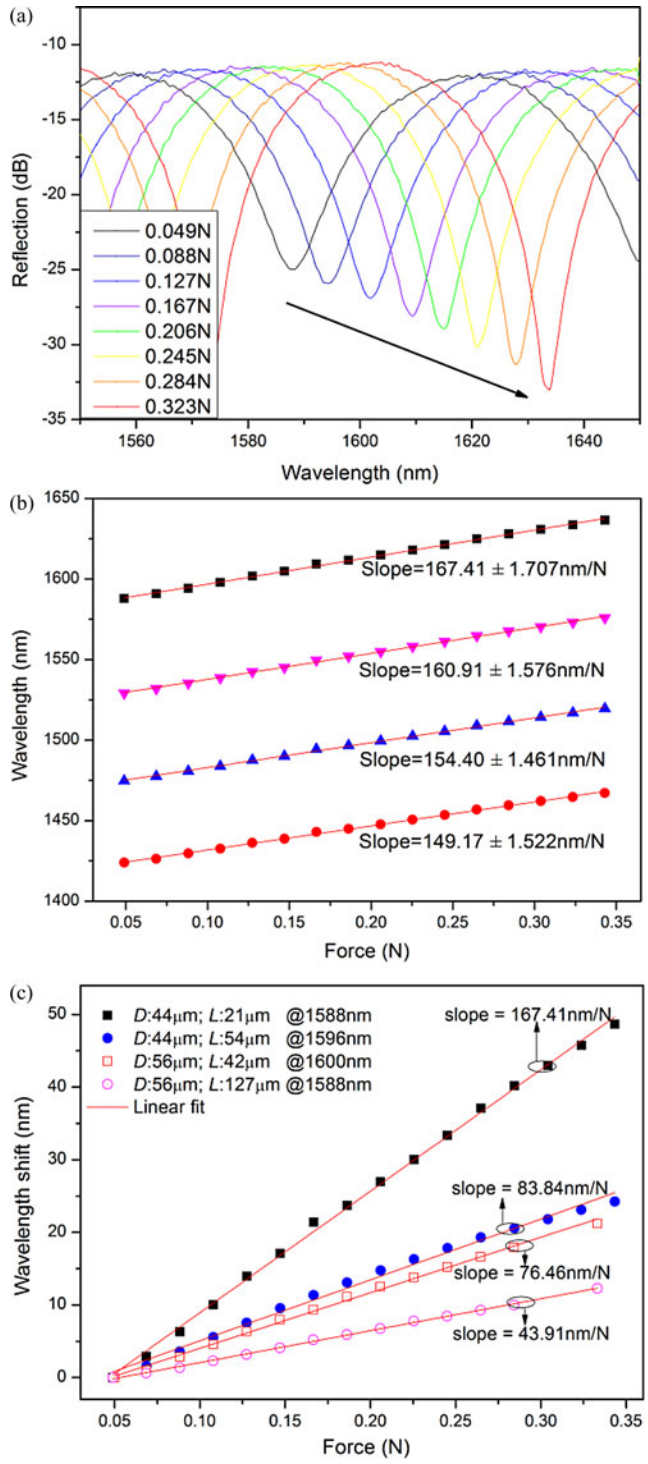

Fig. 5. (a) Reflection spectra and (b) spectral dip wavelength of the MF-enabled FPI with 21 μm cavity length versus applied axial force; (c) Wavelength shift upon applied axial force, for the different FP cavities with different MF diameters D and cavity lengths L.

of the MF-enabled open cavity fabricated with different cavity lengths (~21, 54, 173 μm) and different MF diameters (~44, 56 μm). Fig. 2(d) shows the reflection spectra of the three devices illustrated in Fig. 2(a)–(c). The experimental results show that the spectral fringe visibility decreases with the increment of the cavity length if the two SMF facets are well kept in parallel. Since the FP cavity with 21 μm length deviates from accurate parallel configuration, as shown in Fig. 2(a) and (b), its spectral visibility is smaller than that for the FP cavity with 54 μm length in Fig. 2(d).

TABLE I
FORCE AND RI SENSING CHARACTERISTICS OF THE MF-ENABLED FPIS WITH DIFFERENT MF DIAMETERS AND CAVITY LENGTHS

No.	Microfiber diameter (μm)	cavity Length (μm)	Force sensitivity (nm/N) /dip wavelength(nm)	RI sensitivity (nm/RIU)/ dip wavelength(nm)
1	44	21	167.41/1588	1331/1602
2	44	54	83.92 /1549	1354/1610
3	56	42	78.05 /1600	1284/1592
4	56	127	43.91 /1565	1246/1582
5	56	173	38.45 /1589	1243/1578
6	56	193	36.62 /1663	1314/1618

III. THEORY

Fig. 3 shows the detailed schematic structure of the proposed sensor with a side view microscopic image of the 54 μm-length FP cavity. The incident light propagating through the SMF is respectively reflected by two smooth parallel SMF facets (as cavity mirrors) and interferes with each other in the SMF core resulting in an interference pattern at the output. The reflection coefficients of the two mirrors could be calculated by using the Fresnel reflection formula. Since the reflectivity at the silica/air interfaces is very low (less than 4%) and at the silica/liquid interfaces is much more lower, multiple reflections could be neglected, and the proposed MF-enabled FPI could be modeled simply using the two-beam optical interference equation [23]

$$I = I_{r1} + I_{r2} + 2\sqrt{I_{r1} I_{r2}} \cos\left(\frac{4\pi nL}{\lambda} + \varphi_0\right) \quad (1)$$

where I is the intensity of the interference signal, I_{r1} and I_{r2} are the reflection intensities at the cavity end-faces, respectively, n is the RI of the medium inside the cavity, L is the cavity length, and λ is free-space wavelength. When the phase difference ($\Delta\varphi$) between the two reflection beams satisfied $\Delta\varphi = 4\,\pi nL/\lambda + \varphi_0 = (2m+1)\,\pi$, where m is an integer, spectral dips emerge at the wavelengths satisfying $\lambda_m = 2nL/m$. The fringe spacing or free spectral range (FSR) of the interference spectrum can be expressed as FSR $= \lambda/2nL$. Fig. 2(d) shows three reflection spectra respectively corresponding to different cavity lengths of 21, 54, and 173 μm with 0.049N axial stress under room temperature. As the cavity length increases from 21 to 173 μm, the FSR around 1550 nm decreases from 58.8 to 6.9 nm.

When the MF-enabled FPI is subjected to external perturbations, the wavelength shift can be expressed as [14]

$$\Delta\lambda = \lambda_m\left(\frac{\Delta n}{n} + \frac{\Delta L}{L}\right) \quad (2)$$

where Δn and ΔL are the imposed changes in n and L, respectively. When an axial mechanical force F is applied onto the MF-enabled FPI, the cavity length L is elongated, and the change of cavity length induced by the applied axial force can

TABLE II
COMPARISON OF THE FORCE (STRAIN) AND RI SENSING PERFORMANCES OF FIBER LOOPS, MZIS, AND FPIS FABRICATED USING DIFFERENT METHODS

No.	Fabrication method	Sensing head length	Strain (Force) sensitivity (pm/με)	Around 1.33 RI sensitivity (nm/RIU)	Ref.
1	Hi-Bi PBGBF/ PMFs inside a fiber loop	1.27m/20cm	47.18[5]	63.82[6]	[5,6]
2	Tapering inner air cavity/ S-tapering SMF	860μm/138μm	6.8[9]/~-183[10]	~200[10]	[9,10]
3	Splicing HCR-PCF between SMFs	~13μm	15.4	_	[18]
4	Splicing HC-PCF with SMF	~18μm/~10μm	3.9 [20], 10.3 [21]	_	[20,21]
5	fs laser micromachining on SMF	75μm/~69μm	~6 [22]	1163 [23]	[22,23]
6	FIB micromachining on fiber taper probe	3.5μm	_	110	[24]
7	fs laser drilling and fusion splicing	~60μm	_	994	[27]
8	Splicing SHC-PCF and drilling by fs laser	~50μm	_	851	[28]
9	Splicing microfiber between SMFs with designed relative cross section position	**~21**μm	**~200**	**1331**	**This work**

be expressed as

$$\Delta L\left(F\right) = L\frac{F}{\pi r^2 E} \tag{3}$$

where r is the microfiber radius, E is the Young's modulus of pure silica. Since the RI of the cavity is invariant for the all-opening cavity, the attenuation dip wavelength will shift toward longer wavelength region when certain axial force is applied onto the MF-enabled FPI. In case the FP cavity is filled with RI liquid under constant force, the change of cavity length is negligible and thus the effective RI of the cavity is determined by ambient liquid RI.

IV. SENSING EXPERIMENTS AND DISCUSSION

A. Experimental Setup

Fig. 4 shows the experimental setup of the proposed MF-enabled FPI sensing system. The reflection spectrum of the MF-enabled FPI is measured by employing a homemade supercontinuum light source and an optical spectrum analyzer (OSA: AQ6317B) with a 3dB optical coupler. During the process of reflection spectrum measurement, the MF-enabled FPI is horizontally placed in a temperature controlled oven (TCO) (LCO 102 manufactured by ECOM, Czech Republic). One end of the in-line FPI is fixed, and certain axial force is applied at the other end by loading weights through a fixed pulley. The friction introduced by the pulley is smaller than one thousand of the applied force and, hence, the influence of the friction on the force sensitivity should be very small and could be neglected. The fiber pigtail is coiled by dozens of rings with ∼5 mm diameter.

B. Spectral Response to Applied Axial Force

The axial force sensing characteristics are investigated by loading weights under a constant temperature in air environment. The mechanical strength of the MF-enabled FPI is mainly determined by the MF-SMF joints. With the increment of applied force, the resonant dip wavelengths of the MF-enabled FPIs shift toward longer wavelength region. The FPI with ∼56 μm MF diameter and ∼127 μm cavity length could operate well till ∼0.8N at which one of the MF-SMF joints breaks. Fig. 5(a) shows the reflection spectra of the MF-enabled FPI with ∼21 μm cavity length and ∼44 μm MF diameter under different axial forces. The wavelengths of different spectra dips under different axial forces are shown in Fig. 5(b). Significant red shifts of 43.14, 44.80, 46.71, and 48.65 nm were observed for resonance dips at 1424, 1475, 1529, and 1588 nm, respectively, as applied force increases from 0.049 to 0.343 N. Linear fitting results show that the force sensitivities for the above resonance dips reach about 149.17, 154.40, 160.91, and 167.41 nm/N respectively, with excellent linearity. The remaining MF-enabled FPIs with different MF diameters and cavity lengths (listed in Table I) are also tested. The wavelength responses of different sensing heads are shown in Fig. 5(c). From this figure it is clear that the cavity length and the MF diameter of the MF-enabled FPI have a great impact on the axial force sensitivity.

The variation of the force sensitivities under the same external perturbations can be explained by the Equation (2) and (3). Considering that axial force is applied, the fringes of the MF-enabled FPI will shift according to the following equation:

$$\Delta\lambda = k_{(\mathrm{FP})}\frac{F}{\pi r^2 E} \tag{4}$$

where $k_{(\mathrm{FP})}$ corresponds to the force coefficient. The relationship between the normalized axial force coefficient and both of the MF-enabled FP cavity and SMF parameters can be found in reference [18]

$$\frac{k_{(FP)}}{k_0} = \frac{L + L_{\mathrm{SMF}}}{L + \pi r^2 L/\left(\pi R^2\right)} \tag{5}$$

where R is the SMF radius, L_{SMF} is the SMF length (∼800 mm in our experiment), k_0 corresponds to the axial force coefficient when the MF is replaced by SMF. Since the L_{SMF} has a very small influence on the normalized force coefficient [18] and the radius of SMF is a constant (62.5 μm), the normalized axial force coefficient is mainly determined by the MF radius r and the FP cavity length L. Similar to the experiment results shown in Fig. 5(c), the shorter the cavity length, the higher force sensitivity could be acquired, and the smaller the MF radius, the higher force sensitivity would be achieved. The shorter MF diameter and shorter cavity length a FP cavity possesses, the more sensitive force sensing could be achieved.

According to the relationship between the axial strain and force [10], [20], the force sensitivity of 167.41 nm/N of the MF-enabled FPI with 21 μm cavity length and 44 μm MF diameter is equivalent to the strain sensitivity of ∼200.9 pm/$\mu\varepsilon$, about 13 times of the 15.4 pm/$\mu\varepsilon$ [18] and 51 times of the 3.25 nm/N reported in Ref. [20]. To the best of our knowledge, this force

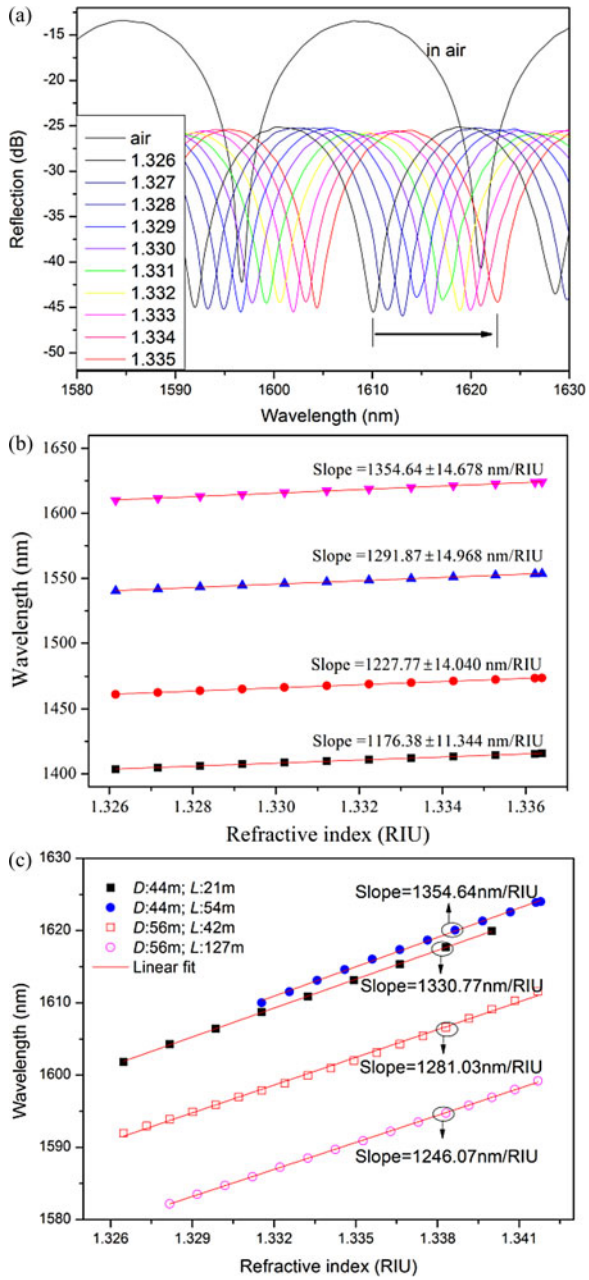

Fig. 6. (a) Reflection spectra and (b) spectral dip wavelength of the FP cavity filled with different refractive index samples as functions of liquid RI; (c) Wavelength shift with different RIs, for the FP cavities with different MF diameters D and cavity lengths L.

sensitivity of the MF-enabled FPI is higher than the all fiber-interferometer-based force sensors ever reported (see Table II).

Due to the asymmetric FP cross section [as shown in Fig. 1(f) and Fig. 2 (a)–(c)], the axial stress applied to the FP cavity will make the cavity facets not in perfect parallel configuration, and thus to change the visibility of the interference spectrum, as shown in Fig. 5(a). In our experiments, the MFs are completely located outside the SMFs core edges by about 5 μm. If the microfiber has a core offset in half from the fiber axis, due to the fusion effect, the interferometric spectral quality will deteriorate dramatically. In case the microfiber is far from the SMF core, the mechanical strength of the FP cavity will reduce because of the stress concentration under the applied force. It is a matter of fact that different MF lateral positions will cause the variation of the axial stress distribution for different cross sections at the MF/SMF joints when the force is applied onto the FPI [17]. Therefore, it will have an influence on the FPI when it is used for force measurement. However, this influence is much weaker than that caused by the change of the MF diameter or the cavity length.

C. Spectral Response to RI

The spectral responses of the MF-enabled FPIs to RI have been experimentally investigated by apply a constant axial force (0.049 N). To test the detailed spectral response around the RI value of 1.33, we use the TCO to control the RI of liquid samples. The liquid sample is n_D = 1.3400 Cargille index-matched oil with an n_D Temp. Coef. = -0.000338/ + °C. The interference spectra of the MF-enabled FPI with ~54 μm cavity length and ~44 μm MF diameter immersed in air and different RI liquid environments are compared in Fig. 6(a), (b) shows the reflection spectral dips at 1403, 1461, 1540, and 1610 nm red shift as ambient RI increases. Linear fitting results indicate that the RI sensitivities for the above spectral dips reach 1176.39, 1227.78, 1291.88, and 1354.64 nm/RIU, respectively, which are comparable to the reported results of 1163 [23], 994 [27] and 851.3 nm/RIU [28]. The spectral responses to RI of different sensors are illustrated in Fig. 6(c). The FP cavities with different cavity lengths and MF diameters have similar RI sensitivities. Here, Equation (2) can be simplified as $\Delta\lambda = \lambda_m(\Delta n/n)$. The RI sensitivity $S_{\rm ri}$, the wavelength shifts $\Delta\lambda$ at dip λ_m driven by RI change Δn is

$$S_{\rm ri} = \frac{\Delta\lambda}{\Delta n} = \frac{\lambda_m}{n}. \tag{6}$$

The experimental results (see Table I) and the Equation (6) indicate that the cavity length and the MF diameter have no influence on the RI sensitivity, which is actually determined by the detectable RI range and the spectral dip wavelength in concern. In a particular RI range, the RI sensitivity could be slightly adjusted by tuning the transmission dip through controlling the applied axial force. The RI sensitivity will slightly decrease when the RI ranges from 1.33 to 1.44. From Equation (6), the RI sensitivities around $n = 1.4$ and $n = 1.44$ are about 1140 and 1110 nm/RIU (at the wavelength of 1600 nm), respectively. Compared with the components fabricated by employing fs laser micromaching [22], [25], this kind of FPI has several advantages, including relatively high extinction ratio, low loss, and prompt access to liquid samples for direct RI measurement. Due to the coarse cavity surface and micro-channels, both of which limit rapid loading of liquid samples and rinse of the cavities reported in Refs. [23], [26]–[28], the sensor presented in this letter would be more suitable for the measurement of liquid RI in real time.

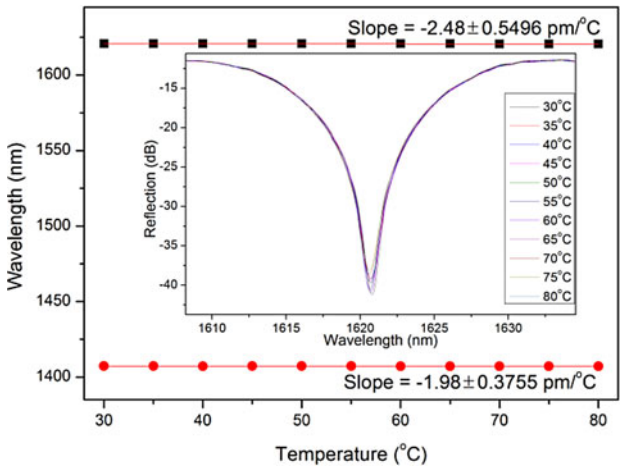

Fig. 7. Spectral dip wavelength of the FP cavity versus environmental temperatures, the inset shows the reflection spectra under different temperatures.

D. Temperature Cross-sensitivities

Since the thermal characteristic of the MF-enabled FPIs is also an important factor that affects the sensor performances in practical applications, we have also investigated the temperature response of the MF-enabled FPI by utilizing an oven. As shown in Fig. 7, the temperature sensitivities of the FPI with 54 μm cavity length obtained by linear fitting are –1.98 pm/°C and -2.48 pm/°C for the dips of 1407 and 1621 nm, respectively. Thus the temperature cross-sensitivities of the MF-FPI to force and RI can be estimated as $\sim 2.96 \times 10^{-5}$ N/°C and $\sim 1.83 \times 10^{-6}$ RIU/°C, respectively. These results confirm that the all-glass structured inline FPIs with air cavities have ultralow temperature dependence as well as temperature cross-sensitivity [22], [23].

V. Conclusion

We have fabricated a novel MF-enabled FPI by combining taper drawing with fusion splicing techniques. This fabrication method to construct an FPI is presented for the first time as far as we know. The ultrahigh force and high RI sensitivities with low temperature cross-sensitivity have been experimentally achieved. The 21 μm-long MF-enabled FI cavity exhibits a force sensitivity of 167.4 nm/N ($\sim$200 pm/$\mu\varepsilon$), which is, to the best of our knowledge, one of the highest values among all the fiber-interferometer-based sensors ever reported so far, and the RI sensitivity of our proposed FP sensor reaches 1330.8 nm/RIU. A study on the force and RI sensitivity dependences upon the MF diameter and cavity length of the MF-enabled FPIs has also been conducted. Both of the experimental results and theoretical analysis indicate that the MF diameter and the cavity length of the MF-enabled FPI have a significant influence on the force response but have no impact on the RI sensitivity of our proposed sensor. Such an MF-enabled FPI has several merits compared with other interferometer-based fiber devices such as high sensitivity, low thermal sensitivity, simple and reconfigurable structure, compact size, and high fringe contrast, which makes it attractive for various sensing and communication applications.

References

[1] M. S. Yoon, H. J. Kim, S. J. Kim, and Y. G. Han, "Influence of the waist diameters on transmission characteristics and strain sensitivity of microtapered long-period fiber gratings," *Opt. Lett.*, vol. 38, no. 15, pp. 2669–2672, Aug. 2013.

[2] W. Luo, J. l. Kou, Y. Chen, F. Xu, and Y. Q. Lu, "Ultra-highly sensitive surface-corrugated microfiber Bragg grating force sensor," *Appl. Phys. Lett.*, vol. 101, no. 13, pp. 133502-1–133502-4, Sep. 2012.

[3] S. M. Tripathi, A. Kumar, R. K. Varshney, Y. B. Pavan Kumar, E. Marin, and J. P. Meunier, "Strain and temperature sensing characteristics of single-mode-multimode-single-mode structures," *J. Lightw. Technol.*, vol. 27, no. 13, pp. 2348–2356, Jul. 2009.

[4] Q. Wu, Y. Semenova, P. Wang, and G. Farrell, "High sensitivity SMS fiber structure based refractometer-analysis and experiment," *Opt. Exp.*, vol. 19, no. 9, pp. 7937–7944, Apr. 2011.

[5] M. S. Ferreira, J. M. Baptista, P. Roy, R. Jamier, S. Fevrier, and O. Frazao, "Highly birefringent photonic bandgap Bragg fiber loop mirror for simultaneous measurement of strain and temperature," *Opt. Lett.*, vol. 36, no. 6, pp. 993–995, Mar. 2011.

[6] C. Zhong, C. Shen, Y. You, J. Chu, X. Zou, X. Dong, Y. Jin, and J. Wang, "A polarization-maintaining fiber loop mirror based sensor for liquid refractive index absolute measurement," *Sensors Actuators B*, vol. 168, pp. 360–364, Jun. 2012.

[7] B. H. Lee, Y. H. Kim, K. S. Park, J. B. Eom, M. J. Kim, B. S. Rho, and H. Y. Choi, "Interferometric fiber optic sensors," *Sensors*, vol. 12, pp. 2467–2486, 2012.

[8] S. Gao, W. Zhang, H. Zhang, P. Geng, W. Lin, B. Liu, Z. Bai, and X. Xue, "Fiber modal interferometer with embedded fiber Bragg grating for simultaneous measurements of refractive index and temperature," *Sensors Actuators B*, vol. 188, pp. 931–936, Nov. 2013.

[9] C. R. Liao, D. N. Wang, and Ying Wang, "Microfiber in-line Mach-Zehnder interferometer for strain sensing," *Opt. Lett.*, vol. 38, no. 5, pp. 757–759, Mar. 2013.

[10] R. Yang, Y. S. Yu, C. Chen, Y. Xue, X. L. Zhang, J. C. Guo, C. Wang, F. Zhu, B. L. Zhang, Q. D. Chen, and H. B. Sun, "S-tapered fiber sensors for highly sensitive measurement of refractive index and axial strain," *J. Lightw. Technol.*, vol. 30, no. 19, pp. 3126–3132, Oct. 2012.

[11] Y. Liu, S. Qu, and Y. Li, "Single microchannel high-temperature fiber sensor by femtosecond laser-induced water breakdown," *Opt. Lett.*, vol. 38, no. 3, pp. 335–337, Feb. 2013.

[12] J. Zhang, Q. Sun, R. Liang, J. Wo, D. Liu, and P. Shum, "Microfiber Fabry-Perot interferometer fabricated by taper-drawing technique and its application as a radio frequency interrogated refractive index sensor," *Opt. Lett.*, vol. 37, no. 14, pp. 2925–2927, Jul. 2012.

[13] S. Pevec and D. Donlagic, "Nanowire-based refractive index sensor on the tip of an optical fiber," *Appl. Phys. Lett.*, vol. 102, no. 21, pp. 213114-1–213114-4, May 2013.

[14] C. Wu, H. Y. Fu, K. K. Qureshi, B. O. Guan, and H. Y. Tam, "High-pressure and high-temperature characteristics of a Fabry-Perot interferometer based on photonic crystal fiber," *Opt. Lett.*, vol. 36, no. 3, pp. 412–414, Feb. 2011.

[15] K. A. Murphy, M. F. Gunther, A. M. Vengsarkar, and R. O. Claus, "Quadrature phase-shifted, extrinsic Fabry-Perot optical fiber sensors," *Opt. Lett.*, vol. 16, no. 4, pp. 274–275, Feb. 1991.

[16] J. S. Sirkis, D. D. Brennan, M. A. Putman, T. A. Berkoff, A. D. Kersey, and E. J. Friebele, "In-line fiber etalon for strain measurement," *Opt. Lett.*, vol. 18, no. 22, pp. 1973–1975, Nov. 1993.

[17] Y. J. Rao, T. Zhu, X. C. Yang, and D. W. Duan, "In-line fiber-optic etalon formed by hollow-core photonic crystal fiber," *Opt. Lett.*, vol. 32, no. 18, pp. 2662–2664, Sep. 2007.

[18] M. S. Ferreira, J. Bierlich, J. Kobelke, K. Schuster, J. L. Santos, and O. Frazao, "Towards the control of highly sensitive Fabry-Perot strain sensor based on hollow-core ring photonic crystal fiber," *Opt. Exp.*, vol. 20, no. 20, pp. 21946–21952, Sep. 2012.

[19] J. Villatoro, V. Finazzi, G. Coviello, and V. Pruneri, "Photonic-crystal-fiber enabled micro-Fabry-Perot interferometer," *Opt. Lett.*, vol. 34, no. 16, pp. 2441–2443, Aug. 2009.

[20] T. Han, Y. Liu, Z. Wang, Z. Wu, S. Wang, and S. Li, "Simultaneous temperature and force measurement using Fabry-Perot interferometer and

bandgap effect of a fluid-filled photonic crystal fiber," *Opt. Exp.*, vol. 20, no. 12, pp. 13320–13325, Jun. 2012.
[21] F. C. Favero, L. Araujo, G. Bouwmans, V. Finazzi, J. Villatoro, and V. Pruneri, "Spheroidal Fabry-Perot microcavities in optical fibers for high-sensitivity sensing," *Opt. Exp.*, vol. 20, no. 7, pp. 7112–7118, Mar. 2012.
[22] Y. Rao, M. Deng, D. Duan, X. Yang, T. Zhu, and G. Cheng, "Micro Fabry-Perot interferometers in silica fibers machined by femtosecond laser," *Opt. Exp.*, vol. 15, no. 21, pp. 14123–14128, Oct. 2007.
[23] T. Wei, Y. Han, H. Tsai, and H. Xiao, "Temperature-insensitive miniaturized fiber inline Fabry-Perot interferometer for highly sensitive refractive index measurement," *Opt. Exp.*, vol. 16, no. 8, pp. 5764–5769, Apr. 2008.
[24] J. Kou, J. Feng, Q. Wang, F. Xu, and Y. Lu, "Microfiber-probe-based ultrasmall interferometric sensor," *Opt. Lett.*, vol. 35, no. 13, pp. 2308–2310, Jul. 2010.
[25] J. Kou, J. Feng, L. Ye, F. Xu, and Y. Lu, "Miniaturized fiber taper reflective interferometer for high temperature measurement," *Opt. Exp.*, vol. 18, no. 13, pp. 14245–14250, Jun. 2010.
[26] T. Wei, Y. Han, H. L. Tsai, and H. Xiao, "Miniaturized fiber inline Fabry-Perot interferometer fabricated with a femtosecond laser," *Opt. Lett.*, vol. 33, no. 6, pp. 536–538, Mar. 2008.
[27] C. R. Liao, T. Y. Hu, and D. N. Wang, "Optical fiber Fabry-Perot interferometer cavity fabricated by femtosecond laser micromachining and fusion splicing for refractive index sensing," *Opt. Exp.*, vol. 20, no. 20, pp. 22813–22818, Sep. 2012.
[28] Y. Wang, D. N. Wang, C. R. Liao, T. Hu, J. Guo, and H. Wei, "Temperature-insensitive refractive index sensing by use of micro Fabry-Perot cavity based on simplified hollow-core photonic crystal fiber," *Opt. Lett.*, vol. 38, no. 3, pp. 269–271, Feb. 2013.
[29] L. Zhang, J. Lou, and L. Tong, "Micro/nanofiber optical sensors," *Photon. sensors*, vol. 1, no. 1, pp. 31–42, 2011.
[30] C. R. Liao, D. N. Wang, and Y. Wang, "Microfiber in-line Mach-Zehnder interferometer for strain sensing," *Opt. Lett.*, vol. 38, no. 5, pp. 757–760, Mar. 2013.
[31] G. Y. Chen, M. Ding, T. P. Newson, and G. Brambilla, "A review of microfiber and nanofiber based optical sensors," *The Open Opt. J.*, vol. 7, pp. 21–57, 2013.
[32] S. Gao, W. Zhang, P. Geng, X. Xue, H. Zhang, and Z. Bai, "Highly sensitive in-fiber refractive index sensor based on down-bitaper seeded up-bitaper pair," *IEEE Photon. Technol. Lett.*, vol. 24, no. 20, pp. 1878–1881, Oct. 2012.

Shecheng Gao received the M.S. degree from Harbin Normal University, Harbin, China, in 2011. He is currently working toward the Ph.D. degree in optics at the Institute of Modern Optics, Nankai University, Tianjin, China.

His research interests include optical fiber devices and its applications in optical sensing and optical communications.

Weigang Zhang received the M.S. degree from the Harbin Institute of Technology, Harbin, China, in 1993, and the Ph.D. degree from Nankai University, Tianjin, China, in 2002.

After receiving the Ph.D. degree, he joined the Institute of Modern Optics, Nankai University, as a Professor. He has more than 100 domestic or international journal publications, two science and technology invention awards, and 21 invention patents. His research interests include fiber gratings, fiber sensors, and fiber network system.

Zhi-Yong Bai received the B.S. degree in theoretical physics from Ningbo University, Ningbo, China, in 2008, and the M.S. degree in optical information propagating and processing from South China Normal University, Guangzhou, China, in 2011. He is currently working toward the PhD. degree in optics fiber sensor at Nankai University, Tianjin, China.

His research interests concentrate primarily on the field in fiber gratings and its applications in optical fiber communication and sensing.

Hao Zhang received the Ph.D. degree from Nankai University, Tianjin, China, in 2005, following work on fiber amplifiers, fiber lasers and their applications.

Since 2005, he has been with the Institute of Modern Optics, Nankai University (IMONK). Following a Postdoctoral appointment at the Imperial College, London, U.K., in 2007, he returned to Nankai University. Since 2010, he has been working as an Associate Professor at IMONK. His current research mainly focuses on acousto-optic interaction in photonic crystal fibers, whispering gallery modes in photonic crystal fibers, fiber-laser-based photonic sensors, and novel fiber grating sensors.

Wei Lin, biography not available at the time of publication.

Li Wang, biography not available at the time of publication.

Jieliang Li, biography not available at the time of publication.